Multilevel system in ac-driven fields: Symmetries and dynamics in a self-assembled quantum lens

Arezky H. Rodríguez,[1,*] L. Meza-Montes,[1] C. Trallero-Giner,[2] and S. E. Ulloa[3]
[1]*Instituto de Física, Universidad Autónoma de Puebla, Apartado Postal J-48, Puebla, Puebla 72570, Mexico*
[2]*Departamento de Física Teórica, Universidad de La Habana, Vedado 10400, Cuba*
[3]*Department of Physics and Astronomy and Nanoscale and Quantum Phenomena Institute, Ohio University, Athens, Ohio 45701-2979, USA*

(Received 19 September 2007; revised manuscript received 30 April 2008; published 3 June 2008)

Theoretical results for single-electron states of lens-shaped self-assembled quantum dots under intense harmonic electric fields are presented. We analyze the time evolution of the system utilizing a nonperturbation Floquet state approach. The full lens geometry is taken into account, allowing us to study the interplay between the spatial asymmetry of the confinement and the magnitude, direction, and frequency of the applied field. Dynamical symmetries and localization are revealed in the structure of Hilbert space of functions and the associated quasienergy spectrum. We discuss the role of the different quasienergy sidebands as the parameters of the system change for light incident parallel and perpendicular to the lens axis. We find that the contribution of different drive harmonics is controlled by fine tuning of field intensity. We further show that avoided crossings in the quasienergy spectrum are correlated with the spectral force of the sidebands and dynamical state localization.

DOI: 10.1103/PhysRevB.77.235405 PACS number(s): 73.21.La, 78.67.Hc, 72.20.Ht

I. INTRODUCTION

The last few years have seen an intense activity on the experimental and theoretical understanding of the dynamical evolution of quantum systems exposed to strong time-dependent external fields. This a problem of important fundamental interest, explored early on by Shirley,[1] as amply discussed in different excellent reviews.[2] Moreover, the topic has acquired a great deal of relevance in connection with the practical operation of devices subjected to oscillating electrical and magnetic fields at the nanoscale. Examples of different physical implementations of the problem have been explored in the shift of resonances in heterostructures as ac fields are applied (the ac-Stark effect),[3] on the behavior of electronic bands in spatially periodic systems,[4–7] and on the production of currents in an ac-driven quantum dot,[8] just to name a few examples.

One important effect in these systems is the strong *dynamical* suppression of tunneling at suitable values of applied ac field. The coherent destruction of tunneling that ensues, known as *dynamical localization* in the literature, has been well studied in two-level systems as coming from the destructive interference introduced by the drive[2,9] and appearing at the crossing of quasienergy levels in the spectrum as a function of driving field amplitude. Other authors have studied the dynamics of a driven particle in a one-dimensional periodic discrete lattice or a superlattice,[10–12] finding that there is dynamical localization whenever the lower miniband collapses, which occurs when the ratio of the Floquet and the laser frequencies are equal to the zeros of the Bessel function J_0. Other works have considered the effect of crossed magnetic fields[13] and the dependence of dynamical localization on the frequency of the drive,[13,14] showing that as the frequency decreases (with respect to the two-level energy spacing), the degree of dynamical localization is reduced. Dynamical localization has been proposed as a tool to control the spatial location of a particle in a two-well potential[2] and to selectively control the tunneling in a multiple-well system.[15] Furthermore, the role of interparticle interactions has been explored in driven systems with different geometries, which include a square quantum dot,[16] a quantum dot molecule,[17,18] and an array of quantum dots.[19]

Zero-dimensional self-assembled quantum dot (SAQD) structures exhibit novel optical and transport properties.[20] Typical growing conditions result in SAQDs with lens shape geometry[21] so that several possible applications underline the importance of analyzing the dependence of this spatial symmetry on their electronic structure.[22] In the present work, we explore the problem of periodic force driving and dynamical localization in a realistic level structure that describes self-assembled quantum dots in semiconductors. As these dots are well described by a lens shape (or dome), we provide a detailed description of the spatial states in that geometry. The principal aims of the present study are

(a) to extend the Floquet formalism to self-assembled quantum dots with lens shape;
(b) to analyze the convergence properties of the basic expansion used in the description of the Floquet states and to establish the importance of incorporating fully the multilevel structure;
(c) to provide a detailed description of the dynamical symmetry properties of states for the two independent directions of the driving electric field with respect to the self-assembled growth direction; and finally,
(d) to identify in this complex level structure the conditions for dynamical localization.

We find the realistic lens shape to be crucial in the description of the dynamics, as the state spatial nonseparability (such as that seen in cylindrical confinement models) plays a relevant role for different field orientations. As we describe below, we observe that the multilevel structure present in typical quantum dots is a vital requirement for the correct description of the dynamical response of carriers. In other

words, we show that it is essential to go well beyond the consideration of only two active levels to fully describe the Floquet quasienergy and the time evolution of realistic quantum dots. Also, we find that even at relatively weak driving forces or frequencies, the description of the dynamics requires the inclusion of many different states in order to achieve a fully converged description of the time evolution.

The importance of taking into account the complete set of eigenstates at zero electric field for a proper description of a periodically driven system has been addressed in different works.[23,24] The study of double quantum well excitonic intersubband transitions in the presence of an intense strong-field terahertz laser showed that under unusual power field intensity the exciton states are strongly "dressed" and oscillate at multiple harmonics of the driving field.[23] Similarly, the dynamical Stark effect in a quantum well within the many-band Kane model was studied in Ref. 24. There, it was shown that the dynamical structure induced in the hole subbands by a strong ac-electric field depends on the amount of admixture in the states at a given value of the wave vector in the Brillouin zone. Nevertheless, the quantum lens geometry in the presence of a periodic force driving potential represents a serious mathematical problem since readily obtainable solutions for the quasieigenstates and quasieigenvalues and their symmetry properties are not known. Moreover, it is important to explore the conditions for dynamical localization to occur in realistic SAQDs under driven strong-field laser.

All of these considerations make the theoretical description of the problem not only much more involved but also much richer. For example, we show that the availability of other states in the real dot system allows the generation of higher harmonics of the driving frequency, with intensity that is fully dependent on the amplitude of the drive, and which could in principle be utilized for its generation.

We find further that despite the complex level structure and associated time evolution, the phenomenon of dynamical localization still remains for suitable values of driving field, although the localization is strongly diminished and appears only partially. We should note that the definition of dynamical localization we use here (the persistence of the system in the initial *state*) is necessarily different from that found in the literature,[10–12] as the confined nonperiodic multilevel system studied here does not allow us to monitor the dynamical evolution in terms of the periodic return to an initial *location*. The multilevel transitions in this nonperiodic quantum system will be shown to be important in this behavior.

The description of the system makes use of a complete analytical solution of the confined states in a general lens geometry, which also allows us to exploit the symmetries of the problem, as we discuss in Sec. II.[25,26] The time-dependent problem uses a mapping to an auxiliary time-independent eigenvalue system via the Floquet theorem for periodic systems.[2] This approach results in the well-known quasienergy spectrum that characterizes the time dependence of the system and allows us to explore the different low- and high-frequency regimes, as well as the effect of driving fields along different directions. In Sec. II, we also elaborate on the role of dynamical symmetries in the problem, and how they give rise to separable sectors in Hilbert space. In Sec. III, we present a systematic study of the dynamics, exploring the behavior of quasienergy spectrum, the role that additional states have in the full description of the response of the system, and how the different state weights vary with applied driving field intensity. We also study the evolution of the system by analyzing the probability of finding it in the initial state as time evolves. Finally, we present a discussion of the results in Sec. IV.

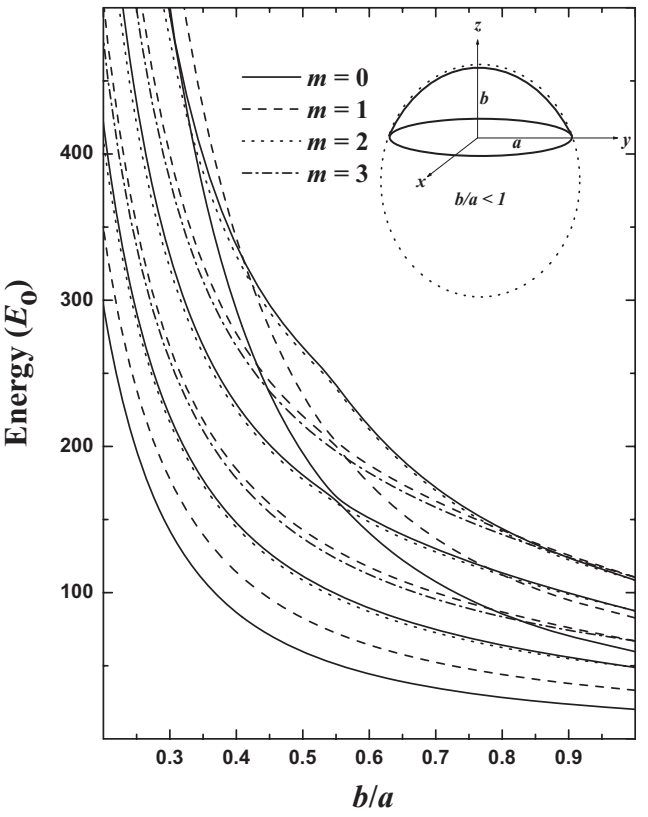

FIG. 1. Single-electron eigenenergies of the lens-shaped self-assembled quantum dot at zero field as a function of the ratio b/a. The inset shows the parameters of the lens. Eigenvalues are plotted with same type of line for a given m subspace, as defined by the quantum number m of the z component of angular momentum; E_0 is introduced in Eq. (5).

II. FLOQUET FORMALISM FOR A QUANTUM LENS

We consider a typical SAQD with lens symmetry of circular cross section of radius a and height b (see inset in Fig. 1), which is harmonically driven by an electric field along the $\hat{\boldsymbol{e}}$ direction with intensity F and frequency ω, $\mathbf{F}=F\hat{\boldsymbol{e}}\sin\omega t$. Assuming that the electron is described by an isotropic band with effective mass m^*, the dynamics of the system is governed by the time-dependent Schrödinger equation,

$$\hat{L}\Psi=\left(-\frac{\hbar^2}{2m^*}\nabla^2-eF\hat{\boldsymbol{e}}\cdot\mathbf{r}\sin\omega t-i\hbar\frac{\partial}{\partial t}\right)\Psi=0, \qquad (1)$$

where the electron is confined in the SAQD domain with a hard-wall potential included here through the boundary conditions.

The Hilbert space $\mathcal{H}$, where the operator $\hat{L}$ of Eq. (1) is defined, corresponds to the direct product of Hilbert subspaces $\mathcal{H}^{(\mathcal{R}_3)}$ and $\mathcal{H}^{(\tau)}$. To the first one belongs the set of bounded functions $\{|\Psi|<\infty\}$ defined in the real space $\mathcal{R}_3$ of the lens, while to the $\mathcal{H}^{(\tau)}$ correspond those periodic functions on time with period $\tau=2\pi/\omega$; thus, $\mathcal{H}=\mathcal{H}^{(\mathcal{R}_3)}\oplus\mathcal{H}^{(\tau)}$. Notice that we focus our attention on the case of single-electron occupation of the dot and ignore the electronic interaction effects that arise for multiparticle occupancy. The growth of SAQD structures with low electron concentration (low and null dopings) is standard so that most dots would have no net charge.[27] Moreover, the charge state can be adjusted by the utilization of gate voltage arrangements.[20]

A. Floquet expansion

The functions belonging to $\mathcal{H}^{(\tau)}$ can be obtained following the standard Floquet theory[2] and the wave function $\psi(\mathbf{r},t)$ is written as

$$\psi(\mathbf{r},t)=\exp(-i\varepsilon t/\hbar)\varphi(\mathbf{r},t), \tag{2}$$

which allows us to rewrite Eq. (1) as

$$\left(-\frac{\hbar^2}{2m^*}\nabla^2-eF\hat{\boldsymbol{e}}\cdot\mathbf{r}\,\sin\,\omega t-i\hbar\frac{\partial}{\partial t}\right)\varphi(\mathbf{r},t)=\varepsilon\varphi(\mathbf{r},t). \tag{3}$$

Here, ε is a real-valued parameter termed the Floquet characteristic exponent or the quasienergy and φ must fulfill the periodic condition $\varphi(\mathbf{r},t)=\varphi(\mathbf{r},t+\tau)$. Following the Floquet theorem for a periodic system, we obtain

$$\varphi(\mathbf{r},t)=\sum_{n=-\infty}^{\infty}\frac{\exp(in\omega t)}{i^n\sqrt{2\pi/\omega}}u_n(\mathbf{r}). \tag{4}$$

Inserting Eq. (4) in Eq. (3) leads to the following equation for the eigenfunctions $u_n(\mathbf{r})$:

$$0=\sum_{n=-\infty}^{\infty}\left\{(\nabla_\rho^2+\lambda-n\Omega)\delta_{n',n}-\xi\hat{\boldsymbol{e}}\cdot\rho\frac{\delta_{n',n-1}+\delta_{n',n+1}}{2}\right\}u_n, \tag{5}$$

where we have introduced the quantities $\rho=\mathbf{r}/a$, $\lambda=\varepsilon/E_o$, $\Omega=\hbar\omega/E_o$, and $\xi=F/F_o$ for the electronic position, quasienergy, field frequency, and intensity, respectively. Here, $F_o=E_o/ea$ and $E_o=\hbar^2/(2m^*a^2)$. Equation (5) is an infinite coupled system of differential equations for $u_n(\rho)$ with eigenvalues $\lambda_n=\lambda-n\Omega$, defined in the $\mathcal{R}_3$ space with a lens symmetry. The lens-shape geometry and the electric field do not allow a closed analytical solution for the eigenfunction u_n. Nevertheless, following the procedure in Refs. 25 and 26, closed solutions for $u_n(\rho)$ can be obtained if the geometric domain of the lens is mapped onto a semispherical one of radius a. Moreover, in the case of hard-wall potentials, the particular conformal mapping reported in Ref. 28 allows us to obtain a complete set of orthonormal eigenfunctions for the space of solutions of Eq. (5).[26] Hence, the set of orthonormal eigenfunctions for the lens geometry at $F=0$, $\{\Phi_{N,m}^{(b/a)}\}$ with eigenvalues $E_{N,m}(b/a)$, is a complete set for the space of solutions u_n. They are expressed in spherical coordinates as

$$\Phi_{N,m}^{(b/a)}(\rho,\theta,\phi)=\frac{f_{N,m}^{(b/a)}(\rho,\theta)}{\sqrt{\rho\,\sin\,\theta}}\frac{\exp(im\phi)}{\sqrt{2\pi}},$$

$$f_{N,m}^{(b/a)}(\rho,\theta)=\sum_{p,l=1}^{\infty}A_{p,l}^{(b/a)}(N,m)\sqrt{\sin\,\Theta_{b/a}}\times\frac{J_{l+1/2}(\mu_p^{(l)}\mathcal{R}_{b/a})}{N_J}\frac{P_l^{|m|}(\cos\,\Theta_{b/a})}{N_P}. \tag{6}$$

The coefficients $A_{p,l}^{(b/a)}(N,m)$ and eigenvalues $E_{N,m}(b/a)$ are solutions of the corresponding eigenvalue problem for a given lens domain with a defined b/a ratio, and the functions $\mathcal{R}_{b/a}(\rho,\theta)$ and $\Theta_{b/a}(\rho,\theta)$ are defined in the Appendix. To ensure the hard-wall Dirichlet boundary conditions on the lens domain, the quantum numbers l and m must fulfill the condition $|l-m|=$odd. N_J and N_P are the norms of the Bessel $J_{l+1/2}$ and generalized Legendre functions $P_l^{|m|}$, respectively, and $\mu_p^{(l)}$ is the pth zero of the $J_{l+1/2}$ function.[29] The number $m=0,\pm1,\pm2,\ldots$ is the projection of the angular momentum along the z axis, which is obviously a good quantum number in this system with axial symmetry. In Fig. 1, the electronic energies $E_{N,m}$ of the lens are plotted as a function of the ratio b/a. Electronic states with $m=0$, 1, 2, and 3 are shown by the solid, dashed, dotted, and dash-dotted lines, respectively, and N (not shown) enumerates, for a fixed value of m, the electronic levels by increasing value of energy. A stronger lens confinement ($b/a\to0$) causes the general increase in the eigenenergies and, as discussed in Ref. 30, even for a very flat lens ($b/a\ll1$), the shape of the confining walls shown in the inset of Fig. 1 is determinant for the states. Note that in the case of quantum dot lenses with $b/a\neq1$, the degeneracy with respect to the quantum number l is broken.

As can be seen from Eq. (3), the function $\varphi_n=\exp(in\omega t)\varphi$ is also a solution with quasienergy $\varepsilon_n=\varepsilon+n\hbar\omega$, where n is an integer number. These additional solutions, a consequence of the time periodicity, have been called "replicas" or "sidebands." In all of our calculations, the same number of replicas will be considered for each quasienergy. By subtracting a suitable integer multiple of $\hbar\omega$, the quasienergy ε is mapped onto the first "Brillouin zone" (FBZ) with $\tilde{E}-\hbar\omega/2\leq\varepsilon<\tilde{E}+\hbar\omega/2$ and $\tilde{E}$ being any real number.[31] The choice of $\tilde{E}$ is arbitrary, and in the following, we take $\tilde{E}=\hbar\omega/2$. Moreover, the quasienergy in the FBZ, in units of $\hbar\omega$, will be scaled to $[0,1]$ for convenience.

On the other hand, notice that the Floquet states at $F=0$ are connected with the wave functions $\Phi_{N,m}^{(b/a)}$ and the quasienergies ε_n with the unperturbed levels $E_{N,m}(b/a)$, respectively, by the relations

$$\varphi_n(\rho,t)|_{F=0}=\exp(in\omega t)\Phi_{N,m}^{(b/a)},$$

$$\varepsilon_n|_{F=0}=E_{N,m}(b/a)+n\hbar\omega. \tag{7}$$

It is clear that the field induces the system to explore different parts of the Hilbert space during its time evolution. How this occurs as a function of time can be analyzed by following the evolution of the wave function, which is written as a linear combination of Floquet states,

$$\Psi(\mathbf{r},t) = \sum_{\{P\}\epsilon FBZ} A_P \psi_P(\mathbf{r},t), \tag{8}$$

with coefficients A_P fixed by the initial conditions. The summation is taken on the FBZ, including all the replicas.

B. Symmetry of the states

In the case of an applied ac-driven field, two independent configurations are possible by choosing properly the direction of the ac field with respect to the axial symmetry $\hat{\mathbf{z}}$ of the lens: (i) $\mathbf{F}\|\hat{\mathbf{z}}$ and (ii) $\mathbf{F}\perp\hat{\mathbf{z}}$. The analysis of the involved symmetries are very useful to interpret the quasienergy spectrum which, as we will see below, contains multiple crossings (arising from states with different symmetries), as well as avoided crossings (or anticrossings) associated with mixing of same-parity states.

1. $\mathbf{F}\|\hat{\mathbf{z}}$

If the ac-field is selected along the z axis, the axial symmetry is preserved, and the Hilbert space of solutions $\mathcal{H}^{(\mathcal{R}_3)}$ splits into orthogonal subspaces $\mathcal{H}_m^{(\mathcal{R}_3)}$ with different z component values of angular momentum $\hbar m$. We have that $\hat{\boldsymbol{\epsilon}}\cdot\mathbf{r} = r\cos\theta$ and, as mentioned above, due to the axial symmetry of the system the space of solutions, $\mathcal{H}^{(\mathcal{R}_3)}$ is separated into orthogonal subspaces $\mathcal{H}_m^{(\mathcal{R}_3)}$, with $m=0,1,2,\ldots$. In the present case, the spatial component u_n in each subspace $\mathcal{H}_m^{(\mathcal{R}_3)}$ can be expanded as a linear combination of the complete set of functions $\{\Phi_{N,m}^{(b/a)}\}$ given by Eq. (6), that is,

$$u_{n,m}(\rho) = \sum_N B_{n,N,m}\Phi_{N,m}^{(b/a)}(\rho). \tag{9}$$

Inserting Eq. (9) into Eq. (5), we have the following time-independent matrix problem:

$$0 = \sum_{N,n} B_{n,N,m}\left\{(\lambda_{N,m}(b/a) + n\Omega - \lambda)\delta_{N',N}\delta_{n',n} - \xi\frac{\delta_{n',n-1}+\delta_{n',n+1}}{2}\mathcal{Z}_m^{(b/a)}(N',N)\right\}, \tag{10}$$

where $\mathcal{Z}_m^{(b/a)}(N',N) = \langle f_{N',m}^{(b/a)}|\rho\cos\theta|f_{N,m}^{(b/a)}\rangle$ and $\lambda_{N,m}(b/a) = E_{N,m}(b/a)/E_o$. Equation (10) is an infinite eigenvalue problem for λ and the weight coefficients $B_{n,N,m}$. We obtained the solutions $u_{n,m}$ in terms of a truncated basis set $\{\Phi_{N,m}^{(b/a)}\}$ ($N=1,\ldots N_{\max}$) by defining a finite eigenvalue linear equation system. The complexity of the problem depends on the values of the parameter ξ but the key issue is related to the convergency of the series in Eq. (9) or equivalently of the equation system (10). An analysis of this important problem is given below.

2. $\mathbf{F}\perp\hat{\mathbf{z}}$

In the case of $\mathbf{F}\perp\hat{\mathbf{z}}$, say, along the x axis, the z component of angular momentum is not a good quantum number. When the ac field is turned on along the x axis, we have $\hat{\boldsymbol{\epsilon}}_x\cdot\mathbf{r} = r\sin\theta\cos\phi$. In this case, the axial symmetry is broken and the spatial component u_n is expanded over all the quantum numbers,

$$u_n(\rho) = \sum_{N,m} C_{n,N,m}\Phi_{N,m}^{(b/a)}(\rho), \tag{11}$$

and we then obtain that

$$0 = \sum_{I=\{n,N,m\}} C_I\left\{(\lambda_{N,m}(b/a) + n\Omega - \lambda)\delta_{I',I} + \xi\frac{\delta_{n',n-1}+\delta_{n',n+1}}{2}\frac{\delta_{m',m-1}+\delta_{m',m+1}}{2}\mathcal{X}^{(b/a)}(N',m';N,m)\right\}, \tag{12}$$

where $\mathcal{X}^{(b/a)}(N',m';N,m) = \langle N',m'|\rho\sin\theta|N,m\rangle$.

The symmetry properties of the operator $\hat{L}$, given by Eq. (1), are related to the generalized parity operator $\hat{S}_{xy}$ defined by $\hat{S}_{xy}:(x\to -x, y\to -y, t\to t+\pi/\omega)$ over the extended Hilbert space of functions, $\mathcal{H}=\mathcal{H}^{(\mathcal{R}_3)}\oplus\mathcal{H}^{(\tau)}$, which includes space and temporal coordinates. According to the commutation relation $[\hat{L},\hat{S}_{xy}]=0$, it follows that the solution $\varphi(\mathbf{r},t)$ presents a definite parity under $\hat{S}_{xy}$ transformation. This allows us to classify the set of solutions into two independent Hilbert subspaces $\mathcal{H}^{(I)}$ ($\mathcal{I}=1,2$) of different symmetries, i.e., $\mathcal{I}=1$ corresponds to states for which $n+m=$even, while $\mathcal{I}=2$ represents those solutions with $n+m=$odd. Then, the matrix (12) can be separated into two blocks of subspaces: one for $n+m=$even and another for $n+m=$odd. Manifestations of these symmetries appear as crossings and anticrossings in the quasienergy spectrum.

III. RESULTS AND DISCUSSIONS

In Fig. 1, the lowest zero-field energy levels are presented as a function of b/a. We now present the resulting quasienergy spectrum for the nonzero field case.

A. ac field along the z axis

When p-polarized radiation is incident parallel to the base plane of the lens, the electric field is turned on along the z direction and the symmetry allows us to separate the operator $\hat{L}$ in blocks; only states with the same quantum number m are coupled. Then, unless specified, calculation of those states within subspaces with $m\neq 0$ will be not shown since all of them present similar behavior. We first explore the dynamics of the system looking at the quasienergy spectrum.

The basis (N,n) in Eq. (10) should contain all the possible states. In practice, the basis is made as large as needed in order to reach the desired convergence in the states. In all our calculations, $n=0,\pm 1,\pm 2,\ldots,\pm 20$, even when for low electric fields full convergence is obtained for a much smaller number of replicas. The quasienergies obtained properly translated to the FBZ are shown in Fig. 2 for the case $b/a=0.91$, $m=0$, and $\Omega=\hbar\omega/E_o=40$ as a function of the dimensionless field intensity $eFa/\hbar\omega$. Notice that for a given size a, since $E_o=\hbar^2/(2m^*a^2)$, Ω specifies the frequency of the ac field $\omega=\hbar\Omega/(2m^*a^2)$ so that $\Omega=40$ is of the order of the level separation in Fig. 1, and in that sense, this value represents a low frequency drive. The labels P in Fig. 2 refer

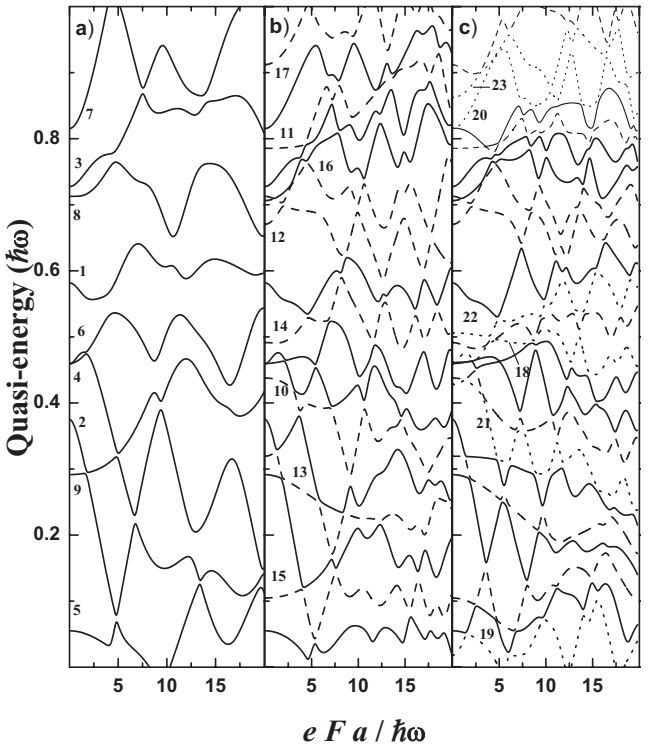

FIG. 2. First Brillouin zone of quasienergies (in units of $\hbar\omega$) as a function of $eFa/\hbar\omega$ (intensity of the ac field) for a fixed dimensionless frequency $\Omega=40$, $m=0$, and $b/a=0.91$. The oscillating field is along the z axis. The labels $P=1,2,3,\ldots$ refer to the Nth eigenvalue of the Hilbert space for vanishing F (see text). The number of lens states at $F=0$ used in the expansion are (a) 9, (b) 17, and (c) 23.

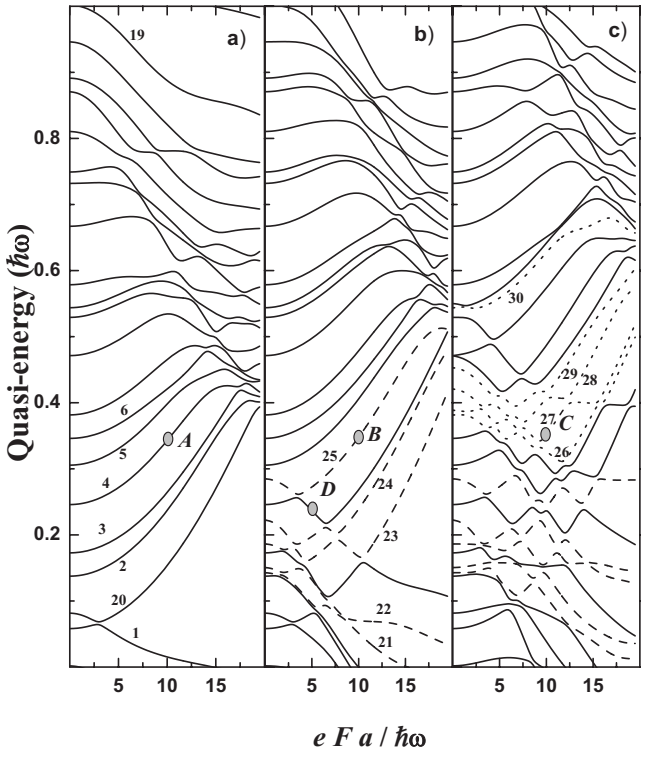

FIG. 3. The same as in Fig. 2 for high frequency $\Omega=400$. The numbers of levels in the expansion are (a) 20, (b) 25, and (c) 30. Points A, B, C, and D are explained in the text.

to the index of the quasienergy at zero field and the number of replica or sideband. Thus, at $F=0$, the label $P\equiv(N,n)$ indicates that the nth replica goes to the zero-field level N as in Eq. (7). The quasienergies in Fig. 2(a) have been calculated including only the lowest nine dot states at $F=0$. Here, at $F=0$, $P=1\equiv(N=1,n=0)$, $2\equiv(N=2,n=-1)$, $3\equiv(N=3,n=-1)$, $4\equiv(N=4,n=-2)$, etc. It can be seen that anticrossings appear due to mixing of states caused by the applied field. For this "soft" lens confinement ($b/a\simeq 1$) and low Ω, we notice that extension of the lens basis to 17 [Fig. 2(b)] and 23 [Fig. 2(c)] states results in a better definition of the lens quasienergies, particularly for higher quasienergies and strong fields. The added lens basis states are shown as the dotted and dashed lines. These plots highlight the importance of having the adequate number of states and their replicas in order to describe the system properly. One should be aware of the fact that including few lens states may be misleading. The observed oscillations of the quasienergies are determined by the repulsion between neighboring levels induced by the electric field. Moreover, additional repulsion is generated by replicas not in the FBZ, as the one occurring at level $P=1$ around $eFa/\hbar\omega=15$ in Fig. 2(a).

As the frequency increases, for example, to $\Omega=400$, in Fig. 3, we observe (and comparing with Fig. 2 where $\Omega=40$) that more lens states at $F=0$ are necessary to achieve a good description. In Figs. 3(a)–3(c), 20, 25, and 30 lens states have been included, respectively. To understand this behavior, we note that larger values of $\Omega=\hbar\omega/E_o$ correspond, for a fixed dot radius a, to higher frequencies of the field. Therefore, the FBZ, $0<\varepsilon\leq\hbar\omega$, is large and more electronic levels $E_{N,m}(b/a)=E_o\lambda_{N,n}$ at $F=0$ are contained inside the BZ. Even for the largest basis, it is evident that many states are necessary since the spectrum is strongly modified when a few states (dashed and dotted lines) are added. Similarly, for a fixed frequency field ω, large Ω corresponds to bigger (larger a) dots, which leads to softer confinement and a stronger effect of the field so that more states are also necessary.

This dependence on Ω is understandable in a perturbation sense, as larger frequency (larger FBZ for a fixed a) would allow transitions to more high-lying states. Similar analysis can be done for the field intensity, where the mixing of the electronic states at $F=0$ increases as the field intensity increases and more states are involved in the complete description of the Floquet quasistates, that is, in the "dressing" of the new state. The behavior at around a given lens eigenvalue (modulo a "replica" energy) will be well described by that state at low fields and frequencies, except near anticrossing points (for those states belonging to the Hilbert subspace). This is indeed clearly observed in the field dispersion in Fig. 2(a), for example, but much less so in Fig. 3 (where only at the lowest fields this is moderately observed).

For a better understanding of the convergence process of the quasienergy dispersion, we provide numerical values of the sequence points A, B, and C in Fig. 3(a)–3(c), respectively. These correspond to the quasienergy levels of 4, 25, and 27 at $eFa/\hbar\omega=10$. If 20 levels are considered, the

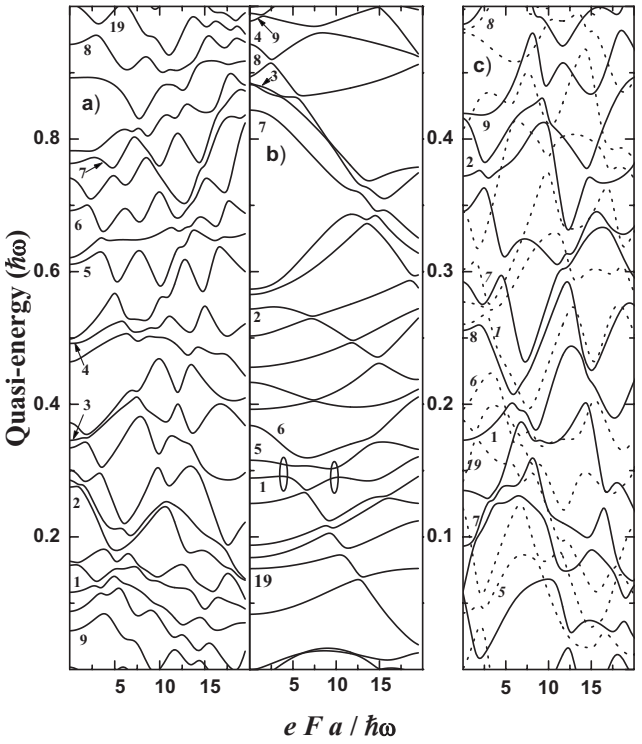

FIG. 4. The same as in Fig. 2 for frequency $\Omega=200$ and (a) $b/a=0.91$, (b) $b/a=0.51$, and (c) $b/a=0.71$. The number of lens states in the expansion is 23. Avoided crossings in panel (b) at $eFa/\hbar\omega=4$ and 9.5 are indicated (see Fig. 6). In (c), the dotted lines correspond to the spectrum for $m=1$. In this panel, we show only the lower half of the first Brillouin zone for clarity.

quasienergy at A has a value of 0.343, while for 25 and 30 levels, we obtain 0.348 and 0.351, respectively. Thus, a good convergence is reached and 20 undressed lens levels are enough for the calculation of this particular quasienergy. Notice that the levels 4, 25, and 27 represent the same state. In contrast, point D in Fig. 3(b) does not even appear at low field ($eFa/\hbar\omega=5$) in Fig. 3(a). To obtain the correct quasienergy dispersion at D, it is necessary to increase the number of basis states to 25. We should also point out that convergence is also quantitatively monitored and understood in terms of the spectral function ρ_P we discuss below.

Let us now fix the number of states in the basis to 23 and the frequency to an intermediate value $\Omega=200$ in order to explore the dependence on confinement. Figures 4(a)–4(c) show the spectra for $b/a=0.91$, $b/a=0.51$, and $b/a=0.71$, respectively. For the strong-confinement regime, $b/a=0.51$ [Fig. 4(b)], the zero-field eigenenergies are higher and have larger separation (see Fig. 1), which results in a "dressed" quasienergy spectrum *with fewer interacting levels* and in flatter field dispersion. Figure 4(c) corresponds to an intermediate regime and the oscillations have larger amplitudes than for stronger quasienergy confinement. For illustration, the quasienergies for $m=1$ are also included in Fig. 4(c). In dotted lines, the spectrum for $m=1$ shows multiple crossings with the $m=0$ levels (continuous lines). These crossings are of course the direct result of the orthogonalization of states with different z components of the angular momentum m, confirming the decomposition of the Hilbert space $H^{(\mathcal{R}_3)}$ in orthogonal subspaces $H_m^{(\mathcal{R}_3)}$.

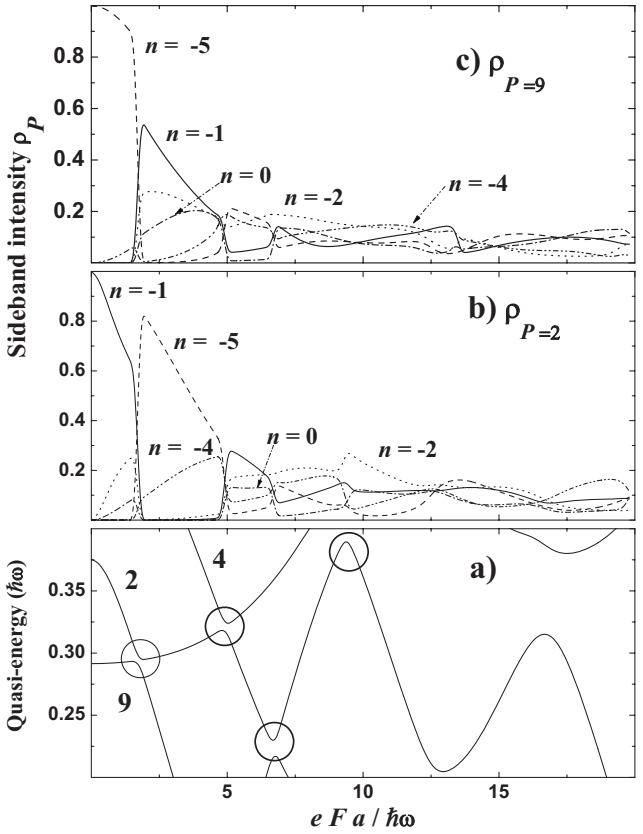

FIG. 5. (a) Small window of the FBZ; the full labels $P=(N,n)$ at $F=0$ of the quasienergies are $2\equiv(2,-1)$, $4\equiv(4,-2)$, and $9\equiv(9,-5)$. Sideband intensities $\rho_P(n)$ for (b) $P=2$ and (c) $P=9$ as a function of $eFa/\hbar\omega$ (intensity of the ac field). System parameters are as in Fig. 2(a): $\Omega=40$ and $b/a=0.91$.

The interaction among different lens levels in the quasienergies as function of the field amplitude can be analyzed in more detail using the sideband intensity or spectral force ρ_P, which amounts to the weight of the nth sidebands on the $\psi_P(r,t)$ Floquet state. Thus, according to expansion (9), the spectral force is given by

$$\rho_P(n)=\sum_N |B_{n,N,m}|^2. \tag{13}$$

Notice that at $F=0$, $\rho_P(n)\equiv\rho_N(n)$. On the other hand, for $F>0$, the spectral force of a given P indicates the weight of the different lens states in the full Floquet expansion (4). Figure 5(a) (bottom panel) shows a small window of the quasienergy spectrum, where some anticrossings have been indicated by the circles. The system parameters are the same as in Fig. 2(a). In Figs. 5(b) and 5(c), the intensity sidebands $\rho_P(n)$ for $P=2$ ($N=2,n=-1$) and $P=9$ ($N=9,n=-5$) have been plotted, respectively, and different n sidebands are shown. The "emission" ($n<0$) weights are stronger than for the $n=0$ replica. We observe the anticrossing between quasienergies $P=2$ and 9 around $eFa/\hbar\omega\simeq 2$. For values up to $eFa/\hbar\omega\simeq 2$, $\rho_{P=2}(n=-1)$ shows a large intensity as expected [continuous line in Fig. 5(b) due to its $F=0$ limit, while $\rho_{P=2}(-5)$ is barely noticeable (dashed line) near $F\simeq 0$]. However, at the anticrossing, a strong mixing of the states

takes place, and $\rho_{P=2}(-5)$ increases rapidly while $\rho_{P=2}(-1)$ decreases for $eFa/\hbar\omega > 2$. Similarly, (dashed line) in Fig. 5(c), the spectral force $\rho_{P=9}(-5)$ is intense for low fields, while $\rho_{P=9}(-1) \simeq 0$ (continuous line) and their strengths are inverted after the anticrossing.

Thus, the spectral weights for $n=-5$ and $n=-1$ are exchanged between the Floquet states at the anticrossing. In the same way, for quasienergy $P=2$, an increasing weight of $n=-2$ is observed for $eFa/\hbar\omega > 5$ [Fig. 5(b)] due to the nearby quasienergy $P=4 \equiv (N=4, n=-2)$. Most importantly, as the field increases, so does the interlevel mixture and the weights of the various replicas become nearly identical so that the amplitude of their contribution are similar. We emphasize that this nearly homogeneous distribution of the spectral force over many different replicas results in substantially different time evolutions of the driven system. We then anticipate that time averages of physical observable could be substantially different from when only the lowest two lens levels are considered.[13]

Let us now see how the system explores different regions of the quasienergies. For simplicity, we consider that the initial state has well-defined z component of the angular momentum in such a way that only states with the same m are considered, and Eq. (8) can be cast in the following way:

$$\Psi_m(\mathbf{r},t) = \sum_N \Delta_N(t)\Phi_{N,m}^{(b/a)}(\mathbf{r}), \tag{14}$$

where

$$\Delta_N(t) = \sum_{\{P\}\epsilon FBZ} \sum_{n=-\infty}^{\infty} A_P B_{n,N,m}(P)\sqrt{\omega/2\pi} \times \exp[i(n\omega t - \pi/2)]\exp(-i\varepsilon t/\hbar). \tag{15}$$

The function $\Delta_N(t)$ contains all the dynamical information due to the presence of the ac electric field. Thus, $P_N(t) = |\Delta_N(t)|^2$ gives, at a given time t, the probability of finding the system in the state $\Phi_{N,m}^{(b/a)}$. Notice that the typical definition of dynamical localization considers the probability that the carrier does not evolve away from its initial spatial state or configuration, as the effective tunneling amplitude from site to site is suppressed.[2] Here, we monitor the dynamical localization by the corresponding quantum probability of finding the particle in its initial state.[32] In what follows, we assume that the initial state is the zero-field ground state $(N=1, m=0)$. We have not explicitly explored other initial configurations but it is likely that the structure of the quasienergy spectrum will give rise to similar dynamical localization behavior in the general case (as it is shown to occur in other systems).[15]

Figures 6(a)–6(d) show the time evolution of $P_1(t)$ during 100 time units, $\tau=\hbar/E_0$, for the strongly confined dot $b/a=0.51$, with $\Omega=200$, and at different values of the field intensity $eFa/\hbar\omega$: 4, 6.5, 9.5, and 14, respectively. According to Eqs. (2) and (8), the wave function is a multiperiod function with strong oscillating behavior, as seen in $P_1(t)$.

The intensities in Figs. 6(a) and 6(c) correspond to the anticrossings in the quasienergy spectrum circled in Fig. 4(b). Clearly, the anticrossings in the quasienergy spectra are correlated with quasilocalization in the Hilbert space for the

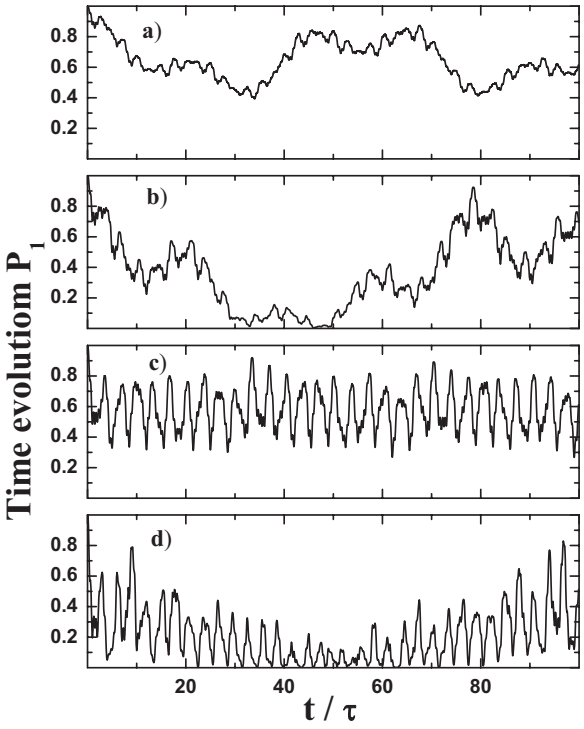

FIG. 6. Time evolution of $P_1(t)$ for different field intensities $eFa/\hbar\omega$: (a) 4, (b) 6.5, (c) 9.5, and (d) 14. System parameters are as in Fig. 4(b), $\Omega=200$ and $b/a=0.51$. Here, $\tau=\hbar/E_o$.

probability of finding the system at the zero-field ground state never goes to zero at fields where anticrossings appear. In contrast, for other field intensities as in Figs. 6(b) and 6(d), $P_1(t)$ reaches small values, even zero. Notice also that the stronger the intensity the lower the values of the probability, a consequence of the strong level mixing as discussed above.

Due to complexity of the multilevel problem, it is not possible to extract the general or analytical criteria for dynamical localization. However, we can be sure that an initial state with the same symmetry properties as the ground state wave function will evolve in a similar fashion, as that shown by $\Delta_N(t)$. In order to quantify the degree of localization, we study the oscillation amplitude (see Fig. 7), defined as $P_1(t=0) - P_{\min}$, where $P_{\min}$ is the minimum value that $P_1(t)$ takes over a long interval of time (100 time units in our case).[16] At zero field, the oscillation amplitude is naturally always zero and increases with the field strength since the latter induces mixing of the states and forces the system to explore larger regions of the Hilbert space away from the initial state. For most of the field intensity range shown, the oscillatory amplitude is near unity, indicating that $P_1(t)$ *vanishes at some time value*, and the probability of the system remaining in the initial state is zero at that instant. However, the oscillation amplitude strongly decreases at some particular field intensities, meaning that $P_1(t)$ never goes to zero at those values, and quasilocalization can be identified. These field values are closely related to anticrossings in the spectrum [see Fig. 4(b)], a remnant of similar behavior in the two-level limit of these problems.[13] Notice, moreover, that as the confinement increases, the field mixes less and less the states that spread

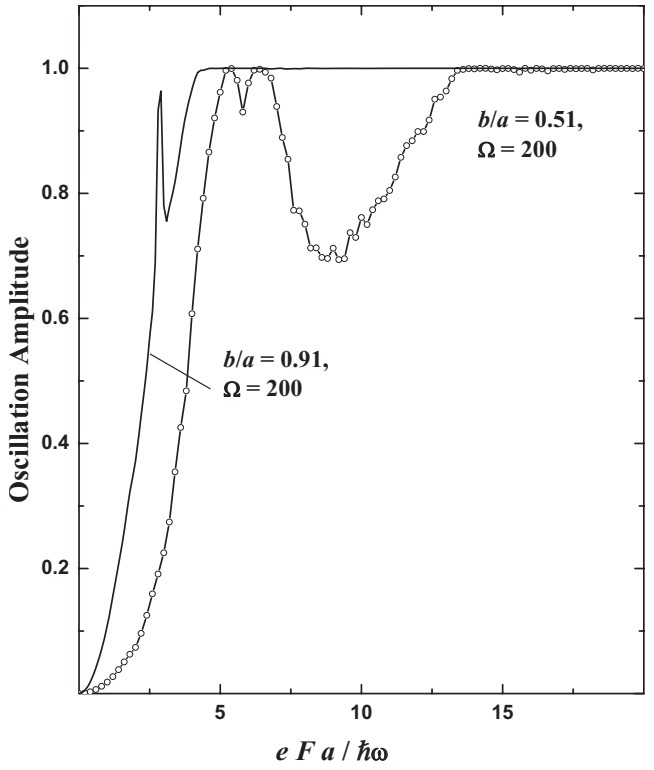

FIG. 7. Oscillation amplitude as a function of the field intensity $eFa/\hbar\omega$ for the dots and frequencies indicated (solid line, $b/a=0.91$ and line with symbols, $b/a=0.51$). Dips in the curves indicate a certain degree of state localization at those field values.

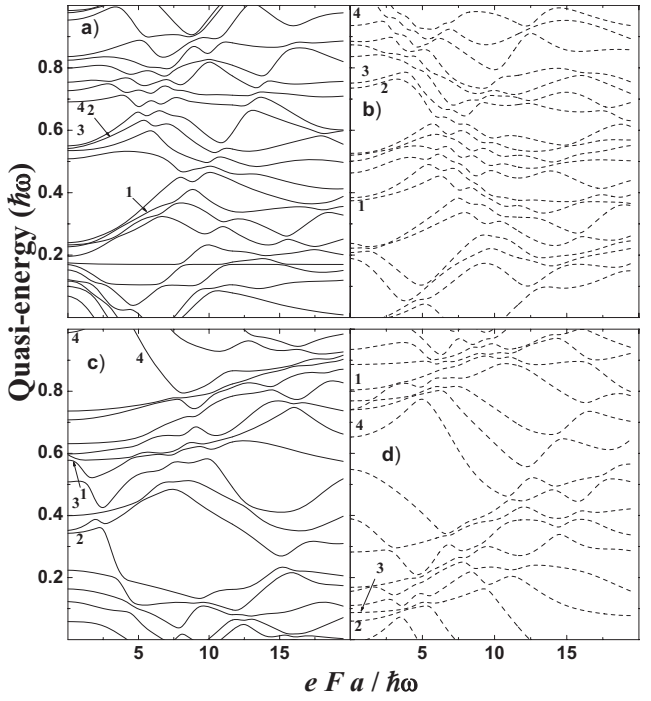

FIG. 8. Quasispectra for fields applied along the x axis. Panels (a) and (b) correspond to $b/a=0.91$, while panels (c) and (d) have $b/a=0.51$. $\Omega=100$ for all panels. Panels (a) and (c) have even symmetry: $m+n=$even and panels (b) and (d) have $m+n=$odd.

apart with confinement and stronger fields are necessary to induce the mixing. Nevertheless, some degree of localization can be observed in both cases, with an overall similar structure. As will be discussed below (Fig. 9), the degree of localization is also sensitive to the value of the drive frequency and decreases for smaller values of Ω.

B. ac field along the x axis

We mentioned above that in the case of a field applied along a direction different from the axial, the rotational symmetry is lost. For normal incidence of the radiation, the electric field is then applied perpendicular to the axis, along x, and dynamical symmetries make the Hilbert space still separable into subspaces such that states follow the conditions $m+n=$even or $m+n=$odd, as discussed above (Sec. II B). Figure 8 confirms this separation in the quasienergy spectra. Figures 8(a) and 8(b) correspond to $b/a=0.91$, where 24 and 16 lens states and their replicas are included, respectively, while for Figs. 8(c) and 8(d), we have $b/a=0.51$ and 15 states in both cases. Frequency $\Omega=100$ in all panels. Figures 8(a) and 8(b) have the same symmetry, $m+n=$even (solid lines), whereas for Figs. 8(c) and 8(d), $m+n=$odd (dashed lines). The labels in the figure refer to behavior of the quasienergy at zero-field energy, similar to the labels in Fig. 2, for example. Here, however, at $F=0$, the label is $P\equiv(N,m,n)$ so that in the panels with even symmetry we have $P=1\equiv(N=1,m=0,n=0)$, $2\equiv(1,2,0)$, $3\equiv(2,0,0)$, and $4\equiv(3,0,0)$ [Fig. 8(a)] and $1\equiv(1,0,0)$, $2\equiv(1,3,-1)$, $3\equiv(2,1,-1)$, and $4\equiv(1,5,-1)$ [Fig. 8(c)]. For the odd symmetry panels, we have $P=1\equiv(1,1,0)$, $2\equiv(1,3,0)$, $3\equiv(2,1,0)$, and $4\equiv(3,1,0)$ [Fig. 8(b)] and $1\equiv(1,1,0)$, $2\equiv(1,2,-1)$, $3\equiv(2,0,-1)$, and $4\equiv(1,4,-1)$ [Fig. 8(d)]. The anticrossings between the quasienergy bands appear in each panel, indicating the coupling of same-symmetry states due to the electric field.

In Fig. 9, we consider the time evolution and compare the oscillation amplitudes for frequency $\Omega=100$ for electric field applied along and perpendicular to the rotational axis of a dot with $b/a=0.51$. As before, larger frequency Ω introduces more quasienergy levels in the Floquet state evolution so that the phases in Eq. (15) oscillate strongly, giving rise to large cancellations, $\Delta_1(t)$ would reach zero and so would $P_1(t)$. As $P_1(t)$ reaches zero at some point, this would lead to higher values of the oscillation amplitude compared to those with small Ω. Figure 9 shows the results for the same frequency and different orientations of the field. We see that the oscillation amplitude for the field along the x axis increases more rapidly at lower field intensities. This can be understood if we consider that the basis consists of the whole spatial space basis and that the field mixing is present over more states than for the z-parallel field case. It is also interesting to notice that the oscillation amplitude shows only monotonic increase and no drop over the range of fields shown, indicating that there is no sign of dynamical localization for this set of parameters. In fact, a comparison of the lower curve here with the dotted-line curve in Fig. 7 for the same lens confinement ($b/a=0.51$) and field direction (along the z axis) but different frequencies Ω (=100 in Fig. 9 vs 200 in Fig. 7) illustrates that the dynamical localization appears more

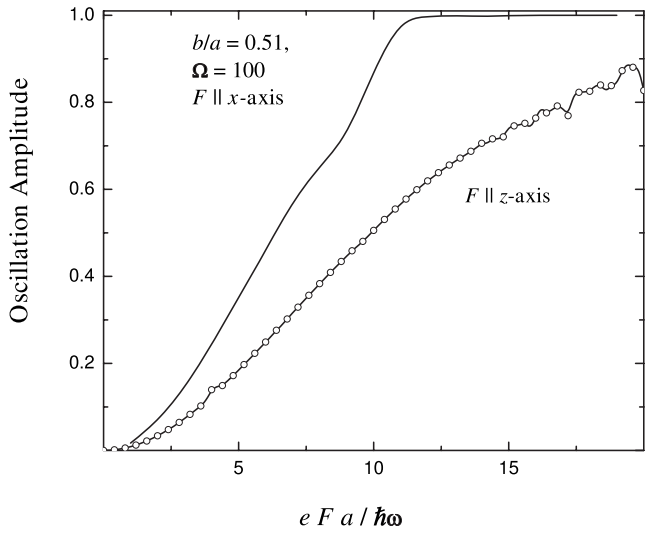

FIG. 9. Oscillation amplitudes as a function of the field intensity $eFa/\hbar\omega$ for a quantum dot lens with $b/a=0.51$. The frequency field is $\Omega=100$ and the two different orientations of the fields is indicated: solid line, F parallel to the x axis and line with symbols, F parallel to z axis.

readily for high frequencies. This behavior is reminiscent of how the dynamical localization at high frequency deteriorates for lower frequencies in two-level systems.[13]

IV. CONCLUSIONS

We have analyzed the time evolution of an electron in self-assembled quantum dots with lens shape in the presence of intense radiation such that the electric field is applied along and perpendicular to the rotational axis of the lens. We have given an explicit analytical representation for the functions defined by Eq. (5) and shown that depending on the direction of the field, the Hilbert space decomposes into subspaces of defined symmetry. For fields along the lens axis, the preserved rotational symmetry allows the solution of the problem for different subspaces. For field direction perpendicular to the dot lens axis, on the other hand, we demonstrate that there is a more general dynamical symmetry and exploit this separation of the Hilbert space to solve this complex time-dependent problem.

This realistic driven single-electron system has been studied over a wide range of frequencies and field amplitudes. We have found and discussed the importance of appropriately considering the complete set of basis functions for convergence of the Floquet states, demonstrating that consideration of the typical two-level approximation yields an incomplete description even at moderate fields and frequencies. We have also calculated the complex quasienergy spectra that result in this problem and analyzed the anticrossings that appear in terms of the interaction among zero-field states and their replicas. We find that these anticrossings are associated with strong shifts in the spectral weights for the Floquet states between two quasienergies, and that for larger field intensities, the spectral weights are distributed homogeneously among a wide range of sidebands. This strong dependence indicates that the appearance of different drive harmonics in the response of the system could be easily controlled by the field strength. It is interesting to consider the possibility of utilizing such lens shape quantum dots in strong ac fields as a source of different harmonics.

In order to study whether dynamical localization prevails under these much more complicated conditions of multilevel dynamics, we have studied the time evolution of the system prepared initially in the zero-field ground state. We find that at field intensities for which a quasienergy anticrossing appears in the spectrum, some degree of state localization is observed; in those circumstances, the probability of finding the system in the initial state never goes completely to zero, but it reaches a minimal value. In that sense, the particle does not return to the initial state with the same frequency of the applied ac electric field. This incomplete dynamical localization has been analyzed quantitatively by means of the oscillation amplitude for different system parameters. Similar to the case of two-level systems, we find that the dynamical localization, already precarious at high frequency, disappears for lower frequency values.

An experiment that would explore the dynamical localization in this multilevel system could be one that investigates differential infrared absorption as the driving field is present (utilizing a Fourier-transform infrared setup). If the particle diffuses away in phase space and essentially abandons the initial ground state, this would directly affect the Fourier transform infrared response. Although such experiment is demanding (considering the requirements of sensitive absorption detection for this single-carrier per dot system), we are hopeful it could be carried out in the near future, as similar experiments are reported in the literature.[33] The analysis and results we present are important for the interpretation of experimental data and suggest further theoretical work to assess the relevance of multilevel structures in realistic systems.

ACKNOWLEDGMENTS

This work was partially supported by CONACyT Project No. E36764 and by the Academia Mexicana de Ciencias and Fundación México, Estados Unidos. C.T.-G. and S.E.U. are grateful for the hospitality at IFUAP and A.H.R. at IF-UNAM, Mexico, where portions of this work were carried out.

APPENDIX: CONFORMAL MAPPING

According to the conformal mapping given in Ref. 26, the functions $\mathcal{R}_{b/a}(\rho,\theta)$ and $\Theta_{b/a}(\rho,\theta)$ are expressed by

$$\mathcal{R}_{b/a}(\rho,\theta)=\sqrt{G_{b/a}^2+S_{b/a}^2}, \tag{A1}$$

$$\Theta_{b/a}(\rho,\theta)=\arctan\left(\frac{G_{b/a}}{S_{b/a}}\right), \tag{A2}$$

where

$$G_{b/a}(\rho,\theta)=\frac{f_+^{1/\alpha}-f_-^{1/\alpha}}{f_+^{1/\alpha}+f_-^{1/\alpha}+2(f_+f_-)^{1/2\alpha}\cos(\phi/\alpha)}, \tag{A3}$$

$$S_{b/a}(\rho,\theta)=\frac{2(f_+f_-)^{1/2\alpha}\sin(\phi/\alpha)}{f_+^{1/\alpha}+f_-^{1/\alpha}+2(f_+f_-)^{1/2\alpha}\cos(\phi/\alpha)}, \quad \text{(A4)}$$

$$f_\pm=1+\rho^2\pm 2\rho\sin(\theta), \quad \text{(A5)}$$

$$\alpha=\frac{\pi/4}{\arctan(b/a)}, \quad \text{(A6)}$$

$$\phi=\arctan\left(\frac{2\rho\cos(\theta)}{1-\rho^2}\right), \quad \rho<1, \quad \text{(A7)}$$

and

$$\phi=\frac{\pi}{2}; \quad \rho=1. \quad \text{(A8)}$$

*Present address: Academia de Matemáticas, Universidad Autónoma de la Ciudad de México, Calzada Ermita Iztapalapa 4163, Del. Iztapalapa 09620, México, D.F., México.

[1] J. H. Shirley, Phys. Rev. **138**, B979 (1965).
[2] M. Grifoni and P. Hänggi, Phys. Rep. **304**, 229 (1998).
[3] A. C. Bittencourt, G. E. Marques, and C. Trallero-Giner, Solid State Commun. **129**, 57 (2004).
[4] K. F. Milfeld and R. E. Wyatt, Phys. Rev. A **27**, 72 (1983).
[5] P. A. Schulz, P. H. Rivera, and N. Studart, Phys. Rev. B **66**, 195310 (2002).
[6] D. F. Martinez, L. E. Reichl, and G. A. Luna-Acosta, Phys. Rev. B **66**, 174306 (2002).
[7] D. Sánchez, G. Platero, and L. L. Bonilla, Phys. Rev. B **63**, 201306(R) (2001).
[8] T. Brandes, R. Aguado, and G. Platero, Phys. Rev. B **69**, 205326 (2004).
[9] F. Grossmann, T. Dittrich, P. Jung, and P. Hänggi, Phys. Rev. Lett. **67**, 516 (1991).
[10] D. H. Dunlap and V. M. Kenkre, Phys. Rev. B **34**, 3625 (1986).
[11] M. Holthaus, Phys. Rev. Lett. **69**, 351 (1992).
[12] M. M. Dignam and C. M. de Sterke, Phys. Rev. Lett. **88**, 046806 (2002).
[13] J. M. Villas-Bôas, W. Zhang, S. E. Ulloa, P. H. Rivera, and N. Studart, Phys. Rev. B **66**, 085325 (2002).
[14] C. E. Creffield, Phys. Rev. B **67**, 165301 (2003).
[15] J. M. Villas-Bôas, S. E. Ulloa, and N. Studart, Phys. Rev. B **70**, 041302(R) (2004).
[16] C. E. Creffield and G. Platero, Phys. Rev. B **66**, 235303 (2002).
[17] P. I. Tamborenea and H. Metiu, Europhys. Lett. **53**, 776 (2001).
[18] C. E. Creffield and G. Platero, Phys. Rev. B **65**, 113304 (2002).
[19] C. E. Creffield and G. Platero, Phys. Rev. B **69**, 165312 (2004).
[20] P. M. Petroff, A. Lorke, and A. Imamoglu, Phys. Today **54** (5), 46 (2001).
[21] See A. D. Yoffe, Adv. Phys. **50**, 1 (2001), and references therein.
[22] See, e.g., S. Lee, J. C. Kim, H. Rho, C. S. Kim, L. M. Smith, H. E. Jackson, J. K. Furdyna, and M. Dobrowolska, Phys. Rev. B **61**, R2405 (2000).
[23] M. Y. Su, S. G. Carter, M. S. Sherwin, A. Huntington, and L. A. Coldren, Phys. Rev. B **67**, 125307 (2003).
[24] A. C. Bittencourt, G. E. Marques, and C. Trallero-Giner, Solid State Commun. **129**, 57 (2004).
[25] C. R. Handy, C. Trallero-Giner, and A. H. Rodriguez, J. Phys. A **34**, 10991 (2001).
[26] A. H. Rodríguez, C. R. Handy, and C. Trallero-Giner, J. Phys.: Condens. Matter **15**, 8465 (2003).
[27] D. J. Eaglesham and M. Cerullo, Phys. Rev. Lett. **64**, 1943 (1990); J. M. Moison, F. Houzay, F. Barthe, L. Leprince, E. Andre, and O. Vatel, Appl. Phys. Lett. **64**, 195 (1996); X. Z. Liao, J. Zou, X. F. Duan, D. J. H. Cockayne, R. Leon, and C. Lobo, Phys. Rev. B **58**, R4235 (1998); J. H. Zhu, K. Brunner, and G. Abstreiter, Appl. Phys. Lett. **72**, 424 (1998).
[28] A. H. Rodríguez, C. Trallero-Giner, S. E. Ulloa, and J. Marín-Antuña, Phys. Rev. B **63**, 125319 (2001).
[29] M. Abramowitz and I. A. Stegun, *Handbook of Mathematical Functions* (Dover, New York, 1972).
[30] A. H. Rodríguez and L. Meza-Montes, Phys. Status Solidi B **243**, 1276 (2006).
[31] H. Sambe, Phys. Rev. A **7**, 2203 (1973).
[32] If one considers a one-dimensional superlattice or discrete lattice problem, the set of two-dimensional functions $|\Phi_{N,m}^{(b/a)}\rangle$ in Eq. (14) has to be modified by the single Wannier functions (Refs. 10 and 12). Under those circumstances, the probability $P_N(t)=|\Delta_N(t)|^2$ is merely the one-dimensional propagator $\psi_N(t)$ given by Eq. (A12) of Ref. 10, and the dynamical localization condition is reached whenever the ratio of the field intensity and the driving frequency is a root of the Bessel function J_0, and the particle returns to its initial position with the ac field period (Refs. 10–12).
[33] Z. Chen, E.-T. Kim, and A. Madhukar, Appl. Phys. Lett. **80**, 2770 (2002).